Macromolecules
ARTICLE
pubs.acs.org/Macromolecules

Access to Nanostructured Hydrogel Networks through Photocured Body-Centered Cubic Block Copolymer Melts

Vincent F. Scalfani and Travis S. Bailey*

Department of Chemical and Biological Engineering and Department of Chemistry, Colorado State University, Fort Collins, Colorado 80523, United States

Supporting Information

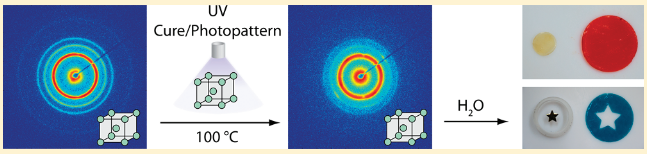

ABSTRACT: Direct access to nanostructured hydrogel networks through high fidelity photocuring of sphere-forming block copolymer melts is demonstrated. Hydrophobic junction points within the hydrogel network are based on an underlying lattice of body-centered cubic spheres (S_{BCC}), produced via melt-state self-assembly of blended AB diblock and ABA triblock copolymer amphiphiles. Integrated thermally stable photocuring chemistry allows for in situ trapping of these spherical domains, independent from the required melt processing necessary to achieve the highly ordered BCC lattice. Swelling of the photocured solids in aqueous (and organic) media afforded highly elastic gels exhibiting excellent mechanical properties ($G' \sim 10^3$ Pa) and complete preservation of the cured solid shape. The hydrogels fabricated in this study were produced from partially epoxidized (19.6%, relative to diene repeat units) blends of polybutadiene-*b*-poly(ethylene oxide) diblock (PB−PEO, $f_{PB} = 0.13$, $M_n = 29\,500$ g mol^{-1}, 88.5 mol %) and PB−PEO−PB triblock ($f_{PB} = 0.13$, $M_n = 59\,000$ g mol^{-1}, 11.5 mol %) copolymers synthesized via anionic polymerization. Addition of UV-activated cationic photoinitiator (4-iodophenyl)diphenylsulfonium triflate (0.5 mol %) produced composite samples exhibiting a highly ordered S_{BCC} morphology after annealing at moderate temperatures (4 h at 80 °C or 60 s at 140 °C) above the PEO melting transition. Composite films (0.33 mm thickness) were then photocured directly from the melt state, postanneal. Cured samples retained the S_{BCC} structure with extremely high fidelity, effectively prestructuring the network of junction points prior to swelling. The photopatterning potential of these uniquely designed hydrogels is also demonstrated.

INTRODUCTION

Hydrogel networks[1−5] are attractive materials in a range of biomedical and biotechnological applications as a result of their potential to provide both mechanical support and sustained permeability (and compatibility) in biologically relevant media.[6] Example applications include intervertebral disk implants, tissue scaffolds,[7−11] cell[12] or molecular[13] encapsulation media, chemical and drug delivery agents,[14,15] and separation membranes.[16−18] Effective performance in these applications, however, is dependent on accurate control over a range of hydrogel characteristics, including elasticity, modulus, mesh size (pore size), mass transfer properties, equilibrium water content, micro- and macroscopic structure (shape preservation), and ease of functional group incorporation.[19] The classic hydrogel frameworks, formed predominately from random physically or chemically cross-linked networks of hydrophilic polymers, are severely limited in this respect, providing limited control over the aforementioned parameters. In these simple systems, the inherently random nature of the cross-linking event produces spatially heterogeneous network connectivity with wide distributions of mesh sizes across the sample. Such heterogeneity is manifested through spatial inconsistencies in mechanical properties, swelling response, and mass transport behavior within the hydrogel.[2] Furthermore, functionalization of the hydrogel can be challenging, as it requires the presence of free reactive sites independent of the exploited cross-linking chemistry. Our group is interested in developing synthetic strategies that overcome these limitations and providing access to spatially homogeneous hydrogel networks with integrated functional group assemblies that can be easily and efficiently modified.

Critical to this mission are hydrogel formation mechanisms that permit active control over the uniformity in the network architecture. In this regard, block copolymers (BCPs) are prime candidates for producing structured hydrogels due to their unique ability to phase separate on the nanometer length scale.[20,21] Of course, the use of ABA block copolymers as solution gelators has been a commonly explored motif in both solvogel and hydrogel research over the past decade or two, particularly in regard to the development of injectable delivery systems. These approaches are based on the formation of micellar networks where hydrophobic A blocks aggregate in solution to form micellar cores and the hydrophilic B midblocks act as tethering elements which span different micelle units. Gelation efficacy in such systems is highly concentration dependent, requiring ABA triblock copolymers to be present in amounts that statistically favor bridging of ABA chains across micelles; dilute solutions favor looping into the same micelle and the formation of

Received: May 23, 2011
Revised: July 7, 2011
Published: July 26, 2011

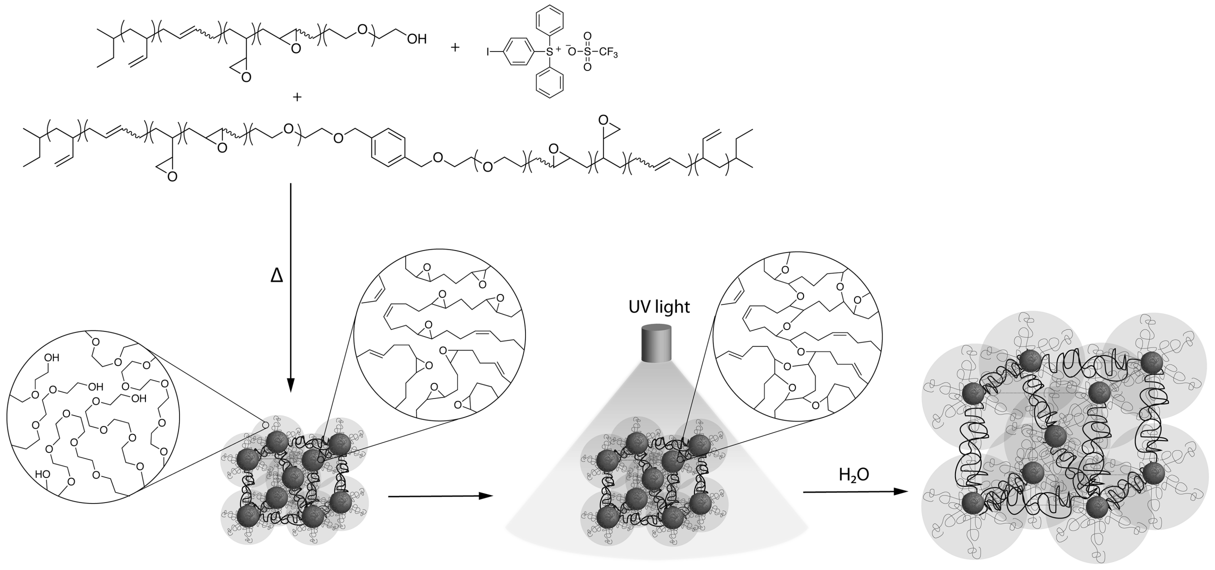

Figure 1. Prestructured hydrogel formation based on spherical forming AB diblock and ABA triblock copolymer melts. Majority component, poly(ethylene oxide), surrounds partially epoxidized polybutadiene spheres and also serves to tether (highlighted in bold) the spherical domains. After melt processing, UV-initiated cross-linking of the epoxide groups with IPDPST cationic photoinitiator solidifies the spheres, resulting in direct trapping of the melt phase morphology. Upon addition of selective solvent for the majority component, an equilibrium swollen elastic network is created, while preserving the preformed structure and shape. The osmotic swelling forces from the selected solvent, the entropic restoring force from the tethering midblock, and the topologically constrained entanglements in those tethers determine the equilibrium swelling dimensions. Magnification circles portray simplified views of the copolymers utilized in this report.

flower-type structures that are unable to contribute to network formation.

Such strategies dramatically improve uniformity in average distance between junction points (micellar cores) but have been used primarily to produce gels systems that are readily deformable with limited elastic character.[6,19,22−24] Such characteristics are consistent with the design constraints for injectable delivery systems but are not particularly useful for more mechanically demanding applications such as membrane separations or biomedical implant technologies. However, this same tethered micelle network motif can be used to form more mechanically robust systems but requires fabrication conditions that produce micelle cores resistant to permanent deformation or failure under load. Ultimately, this amounts to the generation of micelle cores that are sufficiently glassy or rubbery to resist chain pullout under an applied force. Highly entangled, glassy cores can be challenging to produce under solution-based assembly conditions due to plasticization by residually trapped solvents or cosolvents required to temporarily compatibilize the hydrophobic blocks. Postassembly chain extension[25] and cross-linking[26] within the core have been used to enhance elasticity in solution-assembled micelle systems but do require initiation chemistry compatible with the solvating media (typically water) and chain mobility (in the core) consistent with the specific cross-linking mechanism employed.

Recently, our group has developed a new strategy for hydrogel formation using BCPs and tethered micelle networks that is based on prestructuring the gel network in the absence of solvent.[27] The strategy employs blends of sphere-forming AB diblock and ABA triblock copolymers that are melt-processed and subsequently vitrified to preserve their nano- and macroscale structure after cooling. Self-assembly into densely packed spherical aggregates while in the melt state produces a highly regular lattice of spherical junction points, similar to that shown in Figure 1. In aqueous media, the majority component B is selectively solvated, while the minority sphere component A is hydrophobic and remains solid under the solvating conditions. The added ABA triblock, which can be as little as 3 mol %,[27] serves to physically cross-link the spheres in an extended periodic network. Ultimately, the equilibrium swelling dimensions are determined by a balance among solvent-induced osmotic swelling forces, entropic resistance provided by the tethering midblocks, and topologically constrained entanglements among the tether population. This strategy allows precise control over nanoscale structuring prior to swelling, taking advantage of the near-equilibrium conditions produced by annealing in the melt state. Network morphologies and tethering configurations produced by solution-based assembly, in contrast, are often kinetically determined and are therefore susceptible to variations in processing conditions, such as cosolvent removal rates, for example. Prestructuring in the melt state also avoids the inherent concentration dependence of solution-based network formation and eliminates potential trapping of organic cosolvents during the gelation process.

The original systems studied by our group were comprised of poly(styrene)-*b*-poly(ethylene oxide) (PS−PEO) diblock and poly(styrene)-*b*-poly(ethylene oxide)-*b*-poly(styrene) (PS−PEO−PS) triblock copolymers. These model PS−PEO hydrogels validated the ability of our melt blending strategy to provide tunable mechanical properties (through adjustment of triblock copolymer ratio), adjustable pore sizes (length of bridging block), long-term preservation of macroscopic shape, and high-density incorporation of free hydroxyl groups within the hydrogel interior.

Only a few examples exist of using melt-state self-assembly of BCPs to prestructured hydrogel systems.[27−29] Interestingly, in each of these, including our own previous work,[27] vitrified PS was utilized to physically cross-link the system. While the use of vitrification as a physical cross-linking mechanism presents many advantages (simplicity, reprocessability, etc.), reliance on vitrification has significant limitations as well. Glass transition temperatures are extremely sensitive to both domain size and molecular weights below the entanglement limit, which places a lower molecular weight bound on the minority, core forming, blocks. For example, in our previous studies, we found the use of 8 kDa PS[27] with a bulk glass transition of ~80 °C still resulted in hydrogel softening in the 60 °C range. Thus, the use of vitrified core blocks to physically cross-link the system can limit the usage temperatures for the hydrogel formed. Given the significant asymmetry in the block volume fractions required to form sphere-based systems in the melt, such a lower bound on core block molecular weight translates into hydrogel systems with overall block copolymer molecular weights that are very large, that is, on the order of 70 kDa and higher. This, in turn, constrains the hydrogel swelling ratios to large equilibrium values, limiting access to materials with smaller degrees of swelling, often desirable for particular biomedical and drug encapsulation technologies.

Commonly used vitreous core polymers such as PS and polylactide also offer little to no resistance to nonaqueous solvents, limiting the compositional flexibility of swelling media that can be employed. This is particularly problematic when postswelling functionalization chemistries are considered (for example, the addition of small organic moieties, peptide sequences, growth factors, etc.), as the solvent conditions (even aqueous) that can be readily employed without plasticizing the vitrified domains can be highly restrictive. Considering one of the very promising advantages of incorporating AB diblock copolymer into these tethered micelle networks is the natural presentation of readily functionalizable, free chain ends within the hydrogel interior and surface, the exclusive use of vitrified core strategies in tethered micelle-based hydrogels is extremely limiting.

These disadvantages can be overcome through the use of nonvitreous, lower molecular weight BCP systems, in which the core domains can be chemically cross-linked into fixed, rubbery domains. The cross-linking of the core domains removes the lower molecular weight bound on the minority component of the block copolymer, giving access to the full range of possible swelling ratios in these materials, and produces network structures that are resilient in both aqueous and nonaqueous solvent systems. Significant challenges must be met, however, with respect to the cross-linking chemistry adopted. Introduction of any cross-linking agents or functionality to the system must be delicate enough to not disturb the self-assembled structure. The curing chemistry itself must also be able to withstand thermal annealing of the BCP system to moderately high temperature (up to ~200 °C), commonly necessary to generate highly ordered structures. Finally, the curing event must be rapid enough to translate the melt-state morphology to the cured form without disturbing the delicate balance of forces defining the domain geometry established through self-assembly.

Our group has recently demonstrated the use of thermally stable photocuring chemistry that allows BCPs to be thermally processed for extended periods prior to cure, while simultaneously providing high fidelity translation of the melt-state morphology into the postcure solid.[30] We have shown successful selective trapping of multiple morphological states from a single BCP that exhibits thermally dependent order-to-order transitions (OOT). Partially epoxidized polyisoprene-*b*-poly(ethylene oxide) (PI–PEO) BCPs were blended with a thermally stable UV cationic photoinitiator[31,32] (1 mol % (4-iodophenyl)-diphenylsulfonium triflate, IPDPST) and photocured in the melt via UV irradiation as either hexagonally packed cylinders or bicontinuous gyroid. Importantly, the thermal stability of the cationic photoinitiator provides ample melt-state processing time, without any thermally induced, premature initiation of cure. Classic methods for cross-linking BCPs such as thermal free-radical initiated mechanisms or coupling reactions are extremely system dependent and most often do not allow for extended precure processing.[33] These newly developed polydiene-based BCP systems are low molecular weight, highly ordered (pre- and postcure), and chemically cross-linkable. Thus, these systems are ideal candidates for nonvitrified forms of our prestructured hydrogels.

In this report, we demonstrate the versatility of combining this thermally stable photocuring chemistry[30] with AB diblock and ABA triblock copolymer blend-based hydrogels[27] to produce highly elastic, nanostructured, solvent tolerant, and potentially photopatternable hydrogels systems. The hydrogels described herein are comprised of partially epoxidized polybutadiene-*b*-poly(ethylene oxide) (ePB–PEO) BCPs amenable to curing through cationic ring-opening polymerization of the epoxide functionality. The general approach, depicted in Figure 1, requires melt processing blends of ePB–PEO diblock, ePB–PEO–ePB triblock (11.5 mol %), and small amounts of photoinitiator (0.5 mol % IPDPST relative to diene repeat units) into small disks, which are then annealed above the PEO melt transition (65 °C) to facilitate assembly of the targeted body-centered cubic sphere morphology (S_{BCC}). The ordered structure is then exposed to UV light while being held at 100 °C, triggering the curing event and translating the S_{BCC} melt morphology to the cured solid. After curing, pressed discs swell isotropically in solution, with complete preservation of the preswollen shape. Analysis of rheological properties and the demonstration of simple, large-scale photopatterning conclude this report.

RESULTS AND DISCUSSION

Synthesis. A parent PB–PEO diblock copolymer (M_n = 29 500 g mol^{-1}, polydispersity index (PDI) = 1.03) was synthesized according to a previously reported procedure[30,34] using two-step anionic polymerization of butadiene and ethylene oxide monomer. The targeted volume fraction (f_{PB} = 0.13) of PB was confirmed with ^{1}H NMR spectroscopy. PB–PEO–PB triblock copolymer was synthesized by titrating the alcohol end groups on PB–PEO with potassium naphthalenide to form active alkoxides and then slowly adding the coupling agent[35] α,α′-Dibromo-*p*-xylene (1 equiv of PB–PEO: 0.5 equiv of α,α′-dibromo-*p*-xylene). The resulting copolymer mixture was determined to be 89.6 mass % triblock copolymer by size exclusion chromatography peak integrations, which is consistent with typical coupling yields using this agent in other polymer systems.[35] Mixed triblock copolymer product was then codissolved with pure PB–PEO diblock copolymer such that the overall triblock copolymer content of the blend (PB–PEO–11.5) was 11.5 mol %. This value was selected based on experience with our PS-based hydrogels, as a composition that would produce materials with reasonably high swelling ratios and excellent handling characteristics.[27] Notably, at these blend compositions the hydrogels ultimately produced (vide infra) contain a high concentration of hydroxyl-functional free chain ends, providing a

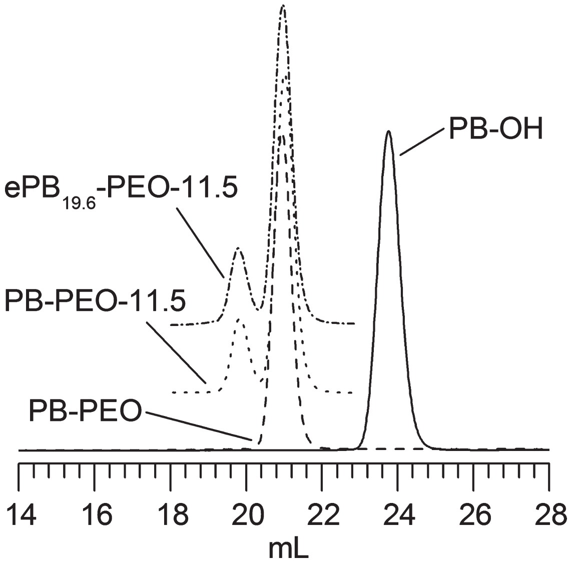

Figure 2. Size exclusion chromatography (SEC) of PB–OH, PB–PEO, PB–PEO–11.5, and ePB$_{19.6}$–PEO–11.5. SEC confirms the absence of PB homopolymer in the PB–PEO diblock. Partial epoxidation is selective without any indication of chain degradation. Near-identical molecular weight distributions were observed. The data for ePB$_{19.6}$–PEO–11.5 and PB–PEO–11.5 have been shifted vertically for clarity.

convenient route toward future hydrogel modification. While the latter is not the subject of this report, the efficient introduction of cross-linking chemistry described directly enables such modifications to be performed in organic environments, if necessary (the demonstration of such modification is the subject of future reports). The olefin repeat units in the PB–PEO–11.5 samples were partially epoxidized (ePB$_{19.6}$–PEO–11.5, 19.6% of butadiene repeat units epoxidized, calculated from ^{1}H NMR integrations) with 3-chloroperoxybenzoic acid (MCPBA), a mild epoxidizing agent. No chain degradation from the MCPBA oxidation was observed as the pre- and postepoxidized products showed identical molecular weight distributions (Figure 2).

Melt State Phase Behavior. The parent PB–PEO (f_{PB} = 0.13) BCP was targeted for its anticipated S_{BCC} morphology,[20,21] which was subsequently confirmed through complementary analysis with small-angle X-ray scattering (SAXS) and dynamic rheology. Melt samples exhibited numerous higher order SAXS diffraction peaks consistent with the S_{BCC} assignment (Figure 3), while dynamic temperature ramp tests exhibited the classic plateau behavior in both the elastic and loss modulus prototypical of cubic (S_{BCC}) BCP phases (Figure 4).[36] The addition of 11.5 mol % triblock, PB–PEO–11.5, had minimal effect on the high degree of order exhibited by the PB–PEO diblock copolymer system; only quantitative changes in the phase behavior were observed with no qualitative differences in the morphology (Figure 5 and Figure S1 show complete SAXS thermal cycle data). Comparing the (110) interplanar spacing determined from the primary scattering wave vector of PB–PEO and PB–PEO–11.5 at 100 °C reveals a slight increase in magnitude from 22.4 to 23.1 nm. The increase in domain spacing with addition of triblock is consistent with previous work from Mai et al.[37] (experimental) and Matsen et al.[38] (mean field calculations), who found small increases in domain spacing in ordered triblock copolymer melts when compared with compositionally equivalent diblock copolymers of half the molecular weight. The phenomenon is attributed to an increase in the elastic properties of the bridging block domains (PEO, here) afforded by the triblock copolymer, although a direct explanation of why this is so remains unanswered, currently.[38]

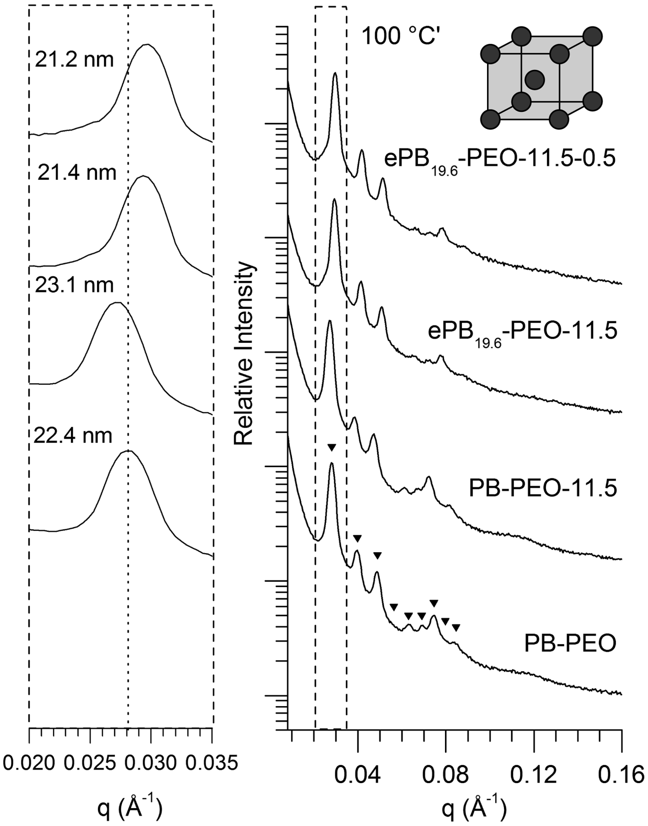

Figure 3. Dependence of *d*-spacing (d_{110}) on the addition of triblock (PB–PEO–11.5), partial epoxidation (ePB$_{19.6}$–PEO–11.5), and incorporation of 0.5 mol % IPDPST cationic photoinitiator (ePB$_{19.6}$–PEO–11.5–0.5) to the parent PB–PEO, all at 100 °C (from cooling). Addition of triblock copolymer increases the plane spacing, while subsequent epoxidation decreases the plane spacing. Incorporation of IPDPST has a negligible effect. All copolymer samples exhibit a highly ordered body-centered cubic spherical S_{BCC} morphology. Inverted triangles represent the location of the allowed reflections for S_{BCC} morphology, based on the position of the primary scattering wave vector $q^* = q_{100}$ (absent for S_{BCC}): q/q^* at $\sqrt{2}$, $\sqrt{4}$, $\sqrt{6}$, $\sqrt{8}$, $\sqrt{10}$, $\sqrt{12}$, $\sqrt{14}$, $\sqrt{16}$, $\sqrt{18}$, etc.

Interestingly, Matsen's previous work predicts that the fraction of triblock copolymers that bridge separate spherical domains (in contrast to looping into the same domain) in pure S_{BCC} forming ABA systems falls impressively in the 75–80% range, although no discussion of the underlying driving force for such high bridging fractions is presented.[38] This is by far the highest value for all the classic morphologies, with lamellar phases being closer to half of that value (~40%). Notably, bridging fractions in blends of ABA triblock and AB diblock copolymer systems, such as those used in this report, have not yet been investigated, experimentally or theoretically, to the best of our knowledge. However, simple comparisons of the unperturbed root-mean-square (rms) end-to-end distance for a PEO chain in the melt, and that which is necessarily imposed on a bridging (or looping) PEO chain through the intersphere distances in the S_{BCC} morphology, reveals the inherent compatibility of bridging

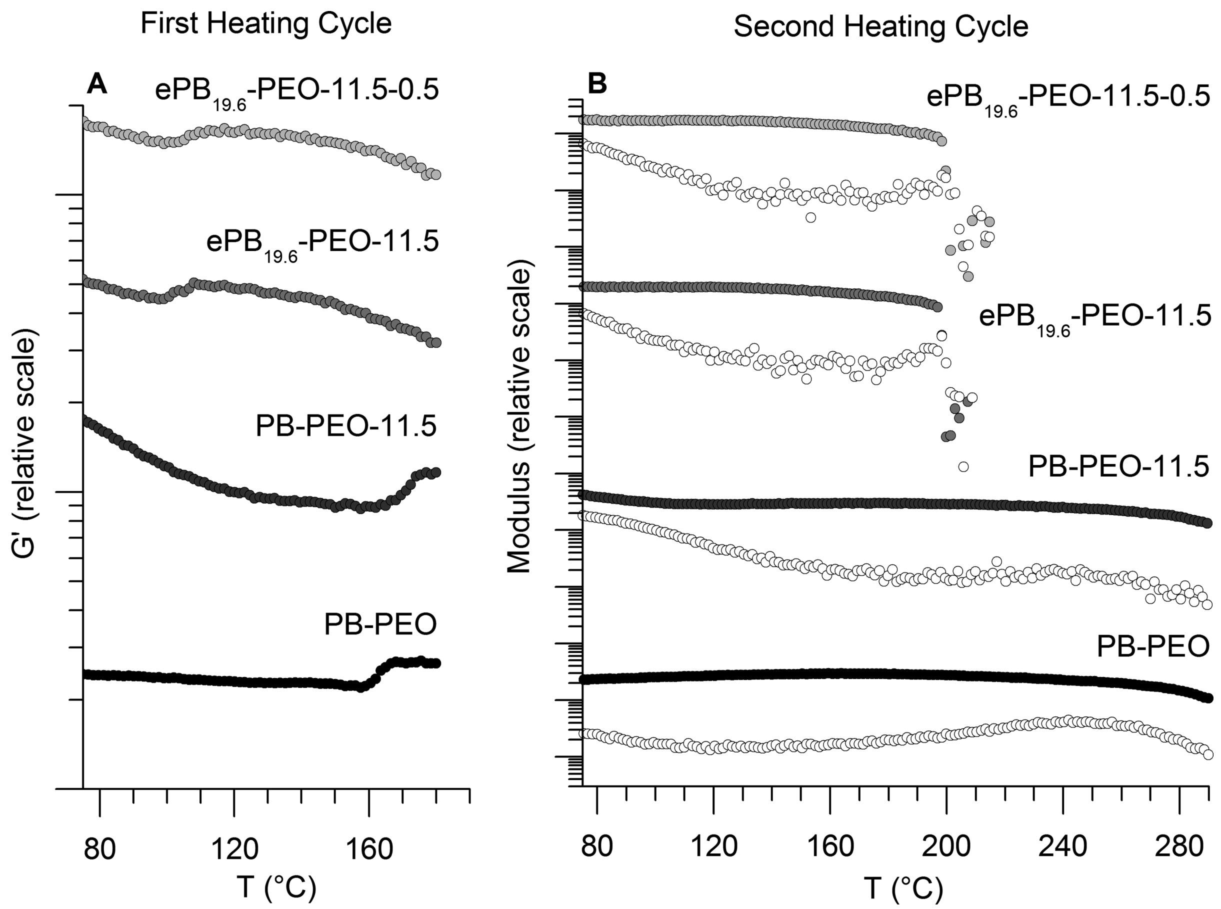

Figure 4. Dynamic temperature ramps of PB−PEO, PB−PEO−11.5, ePB$_{19.6}$−PEO−11.5, and ePB$_{19.6}$−PEO−11.5−0.5 at 1 °C min^{-1} (1 rad s^{-1} and 1% strain). (A) All samples exhibit an initial melt ordered phase consisting of a mixture of the original distorted lamellar-like morphology (PEO crystallization induced) and spherical domains before ordering into pure S$_{BCC}$. Epoxidation has the greatest effect on the temperature at which this phase transition occurs. (B) Second heating cycles (without allowing PEO to crystallize) do not exhibit the distorted L$_C$ phase; only the S$_{BCC}$ morphology is observed for all copolymer samples. Epoxidation drastically lowers the ODT; in contrast, the incorporation of 0.5 mol % IPDPST photoacid (ePB$_{19.6}$−PEO−11.5−0.5) increases the ODT a few degrees.

(vs looping) and appears to support the result of the more elaborate mean field calculations. For example, at 140 °C, an unperturbed PEO chain equivalent in molecular weight to that used in the PB−PEO−PB triblock copolymer blended here (52 400 g/mol), would have a rms end-to-end distance of 20.5 nm.[39] A spherical domain in the S$_{BCC}$ structure has two unique sets of nearest neighbors, both of which are proximal enough to accommodate the other end of a bridging molecule. Analysis of the SAXS data for PB−PEO−11.5 at 140 °C reveals an S$_{BCC}$ structure in which spheres of 15 nm diameters are set on a cubic unit cell of lattice constant a = 30 nm. This produces geometries in which the eight nearest-neighbor spherical domains provide a range of surface-to-surface distances covering 11−41 nm, while the additional six second-nearest neighbors provide a range of surface-to-surface distances from 15 to 45 nm. In combination, the surrounding spherical domains offer tethering chains a broad range of possible end-to-end distances spanning the preferred rms value for PEO. Note that looping offers a chain end-to-end distances from 0 to 15 nm (the full diameter if insertion occurs on the exact opposite side of the sphere), with an average value around 10.6 nm. Thus looping requires a chain to adopt an end-to-end distance much smaller (nearly half) than the preferred rms end-to-end value for PEO. Surely, the excluded volume associated with the spheres themselves places further constraints on the conformational freedom of the tethering chains, but in the absence of that consideration, this simple analysis appears to support the high degrees of bridging predicted by SCFT calculations and apparent in our system. That is, we find only 11.5% triblock copolymer is easily sufficient to achieve full network connectivity in our cured samples.

Both PB−PEO and PB−PEO−11.5 do not exhibit an experimentally accessible (<300 °C) order−disorder transitions (ODTs) as shown in Figure 4B. Partial epoxidation (19.6%) of the PB−PEO−11.5 also produces only quantitative changes in the morphology (Figure S2, complete thermal cycle SAXS data, Supporting Information), with the highly ordered S$_{BCC}$ phase preserved despite modification of the PB backbone. A drastic lowering of the ODT is observed with epoxidation, decreasing from greater than 300 °C in PB−PEO−11.5 to 201 °C in ePB$_{19.6}$−PEO−11.5 (Figure 4B). Comparable behavior was observed in more symmetric PI−PEO BCPs (f_{PI} = 0.61) previously studied by our group, where partial epoxidation lowered transition temperatures from both the cylindrical to gyroid phase (order−order transition) and the gyroid phase to the final disordered state (ODT).[30] At the highest level of

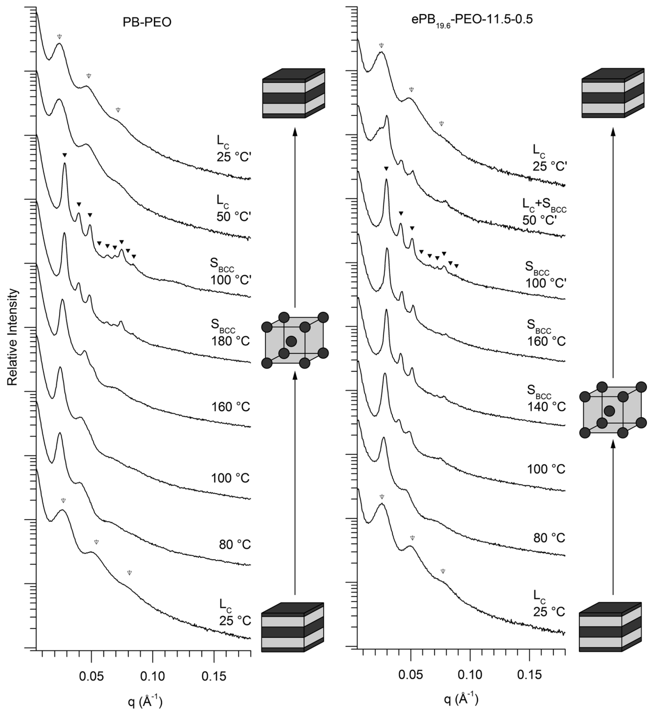

Figure 5. SAXS data of PB−PEO (left) and ePB$_{19.6}$−PEO−11.5−0.5 (right) along a complete heating and cooling (designated with primes) thermal cycle. Morphologies observed during heating include a distorted lamellae-like crystalline phase (L_C), an initial melt phase consisting of a transition between the original distorted lamellar-like morphology and a liquid-like packing of spherical domains, and finally a pure S_{BCC} phase. Upon cooling, a mixed ($L_C + S_{BCC}$) phase is present for ePB$_{19.6}$−PEO−11.5−0.5 before complete adoption of the L_C phase. Inverted triangles represent the location of the allowed reflections for the designated morphology, based on the position of the primary scattering wave vector $q^* = q_{100}$ (absent for S_{BCC}): (L_C) q/q^* at $\sqrt{1}$, $\sqrt{4}$, $\sqrt{9}$, etc.; (S_{BCC}) q/q^* at $\sqrt{2}$, $\sqrt{4}$, $\sqrt{6}$, $\sqrt{8}$, $\sqrt{10}$, $\sqrt{12}$, $\sqrt{14}$, $\sqrt{16}$, $\sqrt{18}$, etc.

epoxidation studied in the PI−PEO system (16.8 mol %), both the OOT and ODT were lowered on the order of 50 °C. Here, epoxidation of spherical forming PB−PEO−11.5 to 19.6% appears to have a much greater influence on the position of the ODT (~100+ °C), perhaps a consequence of the greater compositional asymmetry in combination with the chemical differences between PB and PI. In both PI−PEO and PB−PEO systems, clearly the addition of oxygen into the polydiene domain serves to reduce the Flory-like interaction parameter, χ, without disrupting the qualitative morphological behavior. Epoxidation of the system also reduces the (110) interplanar spacing from 23.1 nm in PB−PEO−11.5 to 21.4 nm in ePB$_{19.6}$−PEO−11.5 (Figure 3). This could be a result of changes in either density or conformational asymmetry of the PB chain upon partial epoxidation, which can directly influence chain aggregation numbers associated with each spherical domain. The addition of 0.5 mol % IPDPST photoacid (ePB$_{19.6}$−PEO−11.5−0.5), in contrast to epoxidation, increases the ODT slightly from 201 to 204 °C. This increase is marginal but is consistent with our previous results, in which the addition of the IPDPST photoacid to epoxidized PI−PEO also resulted in slight increases in OOTs.[30] Again, no qualitative changes were observed in the dynamic rheology or SAXS (Figures 3 and 4) upon addition of the photoacid. The (110) interplanar spacings of ePB$_{19.6}$−PEO−11.5 and ePB$_{19.6}$−PEO−11.5−0.5 were nearly identical at 21.4 and 21.2 nm, respectively.

SAXS data collected for the original diblock copolymer, PB−PEO, and the final cure-ready blend, ePB$_{19.6}$−PEO−11.5−0.5, at multiple temperatures between 25 and 180 °C are depicted in Figure 5. Below the melting point of PEO, the crystalline PEO domains force the structure into a distorted lamellar-like morphology (L_C).[40,41] Upon heating PB−PEO and ePB$_{19.6}$−PEO−11.5−0.5, above the melt transition, the adoption of a true BCC lattice of spherical domains is far from immediate. Instead, the block copolymer samples appear to retain some memory of the original distorted lamellar-like morphology, with an eventual progression to what appears to be a "liquid-like packing" (LLP) of spherical domains.[42−45] After heating past a subtle rheological transition ending at 170 °C for PB−PEO and 110 °C for ePB$_{19.6}$−PEO−11.5−0.5 (see rheology Figure 4A), the copolymer becomes highly ordered with multiple higher order reflections consistent for S_{BCC}, with no indication of any mixed phase morphology. During cooling, the highly ordered S_{BCC} structure is retained until the PEO begins to crystallize ($T_m \sim 65$ °C). With the inception of crystallization of PEO, a mixed phase structure is produced in ePB$_{19.6}$−PEO−11.5−0.5 likely consisting of mixed crystalline lamellae and a distorted form of the original sphere-based structure. After complete cooling at room temperature, only the L_C phase is observed. The mixed behavior consisting of $L_C + S_{BCC}$ upon cooling can be largely attributed to the rapid PEO crystallization-induced distortion of the lattice. Similar behavior for PI−PEO systems have also been reported.[30,40] A region of mixed morphological behavior upon cooling was not observed for the parent PB−PEO. However, after complete cooling of all copolymer samples in this study, no evidence of a residual BCC lattice is observed; only the distorted lamellar-like morphology is present. The subtle transition evident in the rheology near 170 °C for PB−PEO and 110 °C for ePB$_{19.6}$−PEO−11.5−0.5 during heating appears to be related to a transition to a pure S_{BCC} phase. The persistence of the underdeveloped intermediate structure is likely an artifact of slow ordering kinetics during the transition to the energetically preferred S_{BCC} phase and not the product of a true thermodynamic OOT phase transition. This is supported by the eventual development of highly ordered S_{BCC} phases at temperatures below this transition after annealing of ePB$_{19.6}$−PEO−11.5−0.5 at 80 °C (30 °C below the observed mixed lamellae to pure S_{BCC} transition) under vacuum for several hours (Figure S3, Supporting Information). Importantly, this delay in obtaining the pure S_{BCC} morphology is not unique to only the PB−PEO and ePB$_{19.6}$−PEO−11.5−0.5 sample but is observed in all copolymer samples synthesized in this work, including PB−PEO−11.5 and ePB$_{19.6}$−PEO−11.5 with S_{BCC} transitions at 174 and 107 °C, respectively (SAXS shown in Figures S1 and S2, rheology shown in Figure 4A). Notably, such slowly developing S_{BCC} copolymer structures have been previously reported in which there exist sufficient delays during the evolution of the liquid-like packed state and the onset of a fully developed S_{BCC} morphology.[46,47]

Interestingly, there are therefore two distinct ways to melt process the ePB$_{19.6}$−PEO−11.5−0.5 copolymers to obtain a highly ordered S_{BCC} structure prior to curing: either rapidly heat samples above the S_{BCC} transition at 110 °C (Figure 4A) or anneal the system for several hours at a temperature below the observed transition. Importantly, without the excellent thermal stability of the IPDPST photoacid, neither of the aforementioned melt-processing techniques would be possible. The use of photoactivated cationic cross-linking overcomes the thermal instabilities and constraints of many classic cross-linking strategies and provides tremendous flexibility in thermal processing time prior to initiation of cure.[33]

Trapping of the S_{BCC} Morphology in $ePB_{19.6}$–PEO–11.5–0.5. The sufficient delay time in obtaining the pure S_{BCC} morphology has important implications on the melt processing of these materials. It is critical that the system exist as highly ordered S_{BCC} and not as an undeveloped mixture of morphologies. Extended melt processing such as annealing for several hours is time-consuming and has the undesirable consequence of inciting chain degradation if air-free precautions are not taken; it was therefore preferable to rapidly heat above the S_{BCC} transition and then cool the system to the curing temperature. This method afforded minimal processing time and the desired ordered S_{BCC} structure. To cure the S_{BCC} structure, $ePB_{19.6}$–PEO–11.5–0.5 samples were pressed as discs (8.18 mm × 0.33 mm) at 100 °C for 60 s, quenched, and then placed on Kapton film over a Peltier heating element. The disk was then reheated to 140 °C, allowed to soak for 60 s, and then cooled to and held at 100 °C. Some flow deformation of the original disk occurs during this unconfined processing step, such that the disk diameter increases by about 10% (thickness also decreases accordingly). A quartz parallel plate (TA Instruments) was aligned directly over the sample leaving a 0.5 mm gap between the sample and the plate surface. The samples were then exposed for 240 s with broad-spectrum UV light (mercury–xenon lamp, ~100 mW cm^{-2}) using a light guide with a condenser lens aligned ~1 cm from a reflecting mirror within the quartz parallel plate. After cooling, the cured copolymer samples appeared light amber in color, rigid, and insoluble in aqueous or organic solvents (vide infra). Characterization with SAXS confirmed the high fidelity translation of the S_{BCC} morphology to the cured solid (Figure 6), with multiple higher order reflections still present. Within the 110 and 200 diffraction rings, several higher intensity spots indicate the presence of large pseudo-single-crystalline grains within the cured sample. Interestingly, the emergence of such spot patterns during cure has been commonplace, suggesting that cure-induced coarsening of the grain structure may be occurring. However, such phenomena have not been explored in any level of detail.

Similar phase behavior is observed along the entire thermal cycle for both pre- and postcure samples. For example, crystalline, postcured samples also exhibit a similar distorted L_C-like morphology. This is consistent with an elastic distortion of the cured lattice induced by the PEO crystallization event. After heating through the PEO melting transition, the ordered S_{BCC} morphology is again recovered, however, now without any extended annealing, as was required of the uncured samples. The postcured samples exhibit a slightly larger (110) interplanar spacing of 21.8 nm, compared to 21.2 nm in precured samples. Additionally, there is some broadening of the diffraction peaks that suggests a slight smearing of the lattice spacing distribution. This is likely the result of small degrees of temperature heterogeneity during curing, associated with thermal gradients produced from the Peltier heating configuration, the irradiation profile as a function of sample depth, and the exothermic nature of the cationic cross-linking chemistry. However, the persistence of multiple higher order reflections confirms a highly ordered sample is maintained regardless. UV exposure times of 240–360 s (at ~100 mW cm^{-2}) were found to provide mechanically rigid, insoluble solids, all with high translation fidelity (as verified with SAXS).

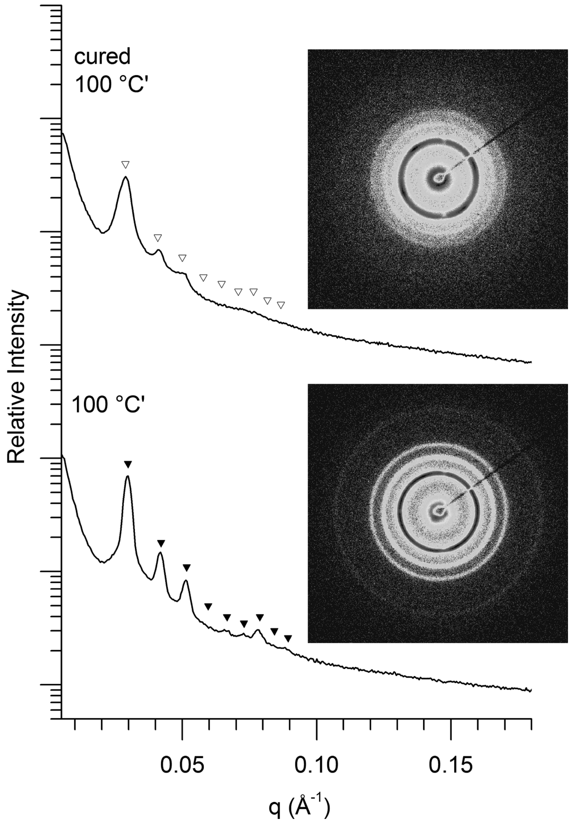

Figure 6. Comparison of SAXS data (collected at 100 °C from cooling) on pre- and postcured $ePB_{19.6}$–PEO–11.5–0.5. Following cure, the $ePB_{19.6}$–PEO–11.5–0.5 solid retains the ordered spherical structure. Inverted triangles represent the location of the allowed reflections for S_{BCC} morphology. Inset pictures are the 2D scattering patterns.

Attempts to quantify the percentage of the epoxide groups reacted through FT-IR and ^{1}H NMR experiments proved quantitatively inconclusive due to significant interference from signals associated with the PEO blocks in the former (Figure S4)[48,49] and insolubility of the samples in the case of the latter. Confirmation of curing was conclusively established through a combination of swelling and rheological experiments. Cured samples retained their disk shape indefinitely when swollen in either water or chloroform, while uncured samples dissolved (or dispersed) within minutes (control experiment) under the same conditions. Because of the isolated nature of the cured core domains, rheological analysis of the melt-state samples (sans solvent), pre- and postcure, could also be performed. A comparison of dynamic temperature ramp behavior (Figure 7) demonstrates both an increased elastic modulus and the clear absence of a disorder transition following cure (thermal degradation is observed for cured samples around 270 °C). Although the majority matrix PEO contributes most of the melt-state rheological character in the sample, the anchoring ends of the tethering blocks become covalently fixed within the spherical domains and change the nature of the material compliance under small strain (1%) oscillatory shear. The inability to disorder is consistent with structural permanence imposed by cured PB domains, which are no longer able to mix with PEO above the original precure ODT around 200 °C. Notably, these results suggests the conversion of epoxide groups during cationic cross-linking

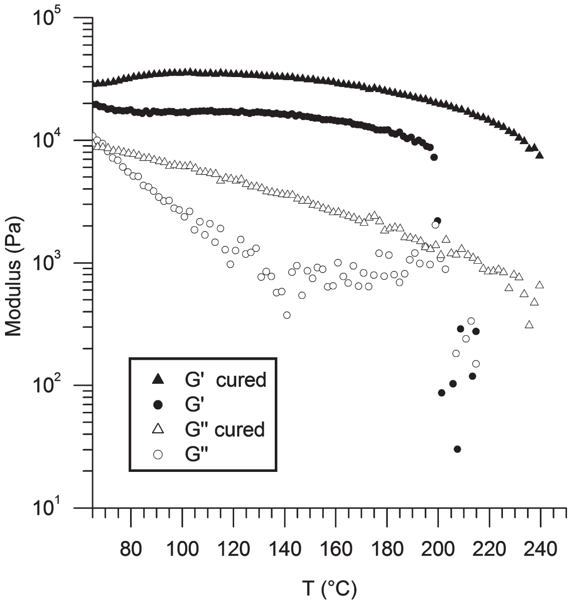

Figure 7. Dynamic temperature ramps of ePB$_{19.6}$−PEO−11.5−0.5 precure (circles) and postcure (triangles) at 1 °C min^{-1} (1 rad s^{-1} and 1% strain). The cured sample exhibits a slightly higher modulus, with the absence of an order-to-disorder transition observed in the uncured sample.

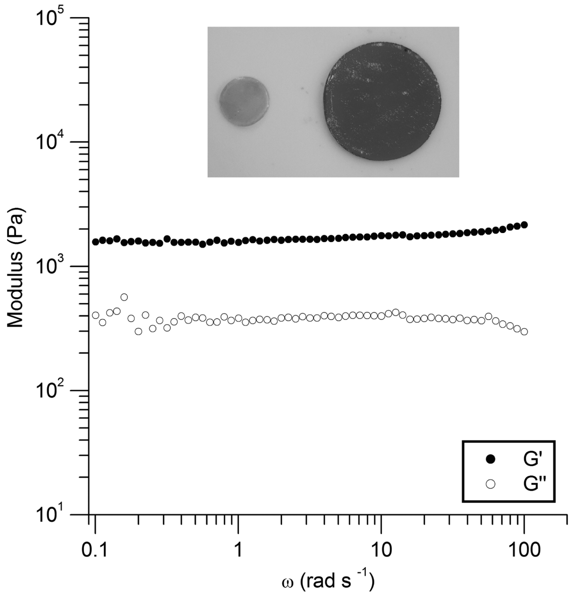

Figure 8. Dynamic frequency dependence of a swollen ePB$_{19.6}$−PEO−11.5−0.5 hydrogel under oscillatory shear at room temperature. Inset photograph shows the relative size of preswollen and postswollen hydrogel. The hydrogel was dyed for photographic clarity.

at these cure times, while not currently quantifiable, is at least sufficient to permanently fix the ePB domains.

Swelling Behavior of Cured ePB$_{19.6}$−PEO−11.5−0.5. After curing, a disk of ePB$_{19.6}$−PEO−11.5−0.5 was placed in DI water. Swelling was obvious within several seconds, with equilibrium dimensions established within ~1 h (determined by point at which there was consistent size and mass of the gel). The swelling was isotropic and preserved the original disk shape. The dry (cured) polymer disk had a volume of 17.3 mm^3, which swelled to a final value of 182.2 mm^3 upon reaching its equilibrium swollen dimensions. This volumetric swelling ratio of 10.5, together with the measured increase in hydrogel diameter (relative to the dry sample) of 2.19, is consistent with perfectly isotropic swelling expected for the S_{BCC} lattice. Mechanical performance of the hydrogel was examined by probing the dynamic mechanical response of the gel at room temperature under oscillatory shear (Figure 8). The elastic (G') and loss (G'') moduli both exhibit near frequency independence over the range of 0.1−50 rad s^{-1}, with a 5-fold difference in magnitude between the two moduli. This behavior is typical of elastic solids and consistent with the behavior observed for our PS-based hydrogel systems previously reported.[27] As expected, the hydrogel modulus (Figure 8) is reduced relative to that found for the cured, but unswollen melt (Figure 7). Simple rubber elasticity theory predicts a modulus of the swollen hydrogel dependent on temperature (T), the polymer volume fraction (ϕ_2), and the number of effective strands (ν_e) per unit dry polymer volume (V_0), with the reduction in modulus due to solvent uptake entirely accounted for by the polymer volume fraction to the one-third power:

$$\text{modulus} \propto T{\phi_2}^{1/3}\left(\frac{\nu_e}{V_0}\right) \quad (1)$$

However, the decrease in modulus measured is significantly greater (~90%) than that predicted (~45%) considering the solvent uptake alone, given a ϕ_2 value of 0.095. This result is actually consistent with our previous work in which found that the number of triblock copolymer molecules in the sample grossly underestimates the number of effective strands in the system. Effective strands involve any polymer segments contributing to the network, and simply counting triblock copolymer molecules fails to account for a large number of additional entanglements in the system. We have found these additional entanglements have a significant effect on the modulus of the swollen and unswollen networks. The source of these entanglements is largely twofold: those produced when topologically constrained triblocks have adopted paths that force direct tether interaction upon swelling and those produced through significant coronal layer overlap between the dangling (nontethered) PEO chains coating the spherical domains. In our continued work on the PS−PEO system, we have found that these coronal layer entanglements can account for roughly 90% of the overall modulus and are a critical component of the mechanical performance of tethered micelle networks. In the current system, the large decrease in modulus upon swelling (relative to the unswollen melt) is thus likely the result of a concurrent decrease in the number of (or relaxation times associated with) effective coronal layer entanglements upon introduction of solvent. At higher frequencies above 50 rad s^{-1}, there is a slight increase in the elastic modulus and a slight decrease in the loss modulus. This increase in elastic character may be the result of topological entanglements (present between tethering midblocks) becoming more relevant at higher frequencies.

In an attempt to characterize the impact of swelling on the S_{BCC} lattice, the ePB$_{19.6}$−PEO−11.5−0.5 hydrogel formed was swollen to equilibrium dimensions, sealed in an airtight Kapton cell, and analyzed via SAXS (Figure 9). In its swollen state, both transmittance and electron density contrast are severely reduced, and the signal-to-noise ratio is such that very long exposure times (12 h) were required to produce the data plotted in Figure 8. Despite unfavorable scattering conditions, a primary scattering peak is quite discernible. Comparison of the pre- and postswollen

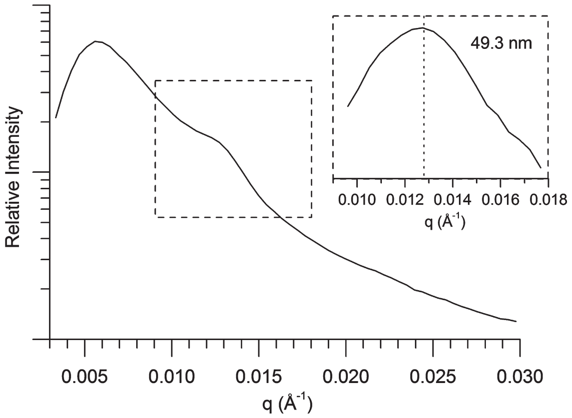

Figure 9. SAXS data for the ePB$_{19.6}$−PEO−11.5−0.5 cured hydrogel, collected at room temperature over a 12 h exposure. Inset contains the background subtracted primary peak, which has a peak maximum at 49.3 nm.

lattice constants (21.8 and 49.3 nm, respectively) calculated from their respective primary scattering vectors suggests a swelling ratio of 2.26, in excellent agreement with that predicted via direct measurement (2.19). The appearance of a primary scattering peak suggests, at the very minimum, that the hydrogel has short-range order in the equilibrium-swollen state, and more importantly, the intersphere distances are highly uniform over macroscopic distances within the sample. Whether the spherical domains within the hydrogel retain average positions that continue to lie on a BCC lattice cannot be discerned using such long exposure times and reduced lab source intensities; future investigations with synchrotron source SAXS and USAXS will be required.

Photopatterning of ePB$_{19.6}$−PEO−11.5−0.5. An extremely interesting consequence of the use of photocuring chemistry to fix the hydrogel structure is the inherent capability to simultaneous photopattern the hydrogels three-dimensionally. To demonstrate the potential of ePB−PEO-based block copolymers in photopatterning applications, an opaque star mask was applied on the surface of the quartz curing attachment. A slightly larger disk (12.8 mm diameter × 0.4 mm thickness) of ePB$_{19.6}$−PEO−11.5−0.5 was subjected to the same aforementioned thermal treatment (heat to 140 °C before cooling to 100 °C) and then exposed to broad spectrum UV light for 300 s. After cooling, the disk appeared amber with a white star in the middle. The polymer disk was allowed to swell in water, and the uncured star dissolved as the disk swelled (Figure 10). Notably, the swollen pattern is much larger than the star mask. However, the shape is preserved, with the only difference being an isotropic expansion of the star shape void (∼2× its original size from star point to point). The ability to wash away masked patterns with aqueous or organic solvents not only provides convincing evidence of the curing efficacy but also serves as a promising launching point for more advanced photopatterning experiments with these materials. Current experiments establishing limits in patterning resolution and line width roughness are underway.

Conclusions. Prestructuring hydrogels from the melt state of self-assembled copolymers has now been extended to chemically cross-linked PB−PEO systems. Previously, this method was limited to physically cross-linked glassy polymers.[27−29] In addition, thermally stable photocuring chemistry, with the use of a cationic photoinitiator, has now been shown to successfully cure BCC spheres (this report), hexagonally packed cylinders,[30] and bicontinuous gyroid[30] morphologies in BCP melt systems. The highly ordered sphere forming systems (S$_{BCC}$) cured in this report, comprised of partially epoxidized PB−PEO diblock and PB−PEO−PB triblock copolymers, provide a facile means of prestructuring the hydrogel network morphology with precise, self-assembly based control. Cured discs swelled in water and chloroform, exhibited excellent mechanical properties in their swollen state, and preserved their macroscopic shape upon swelling. Lastly, the potential for simultaneous photopatterning during cure was demonstrated via the use of a simple mask, opening the possibility for more complex photopatterning applications.

Figure 10. Photopatterned ePB$_{19.6}$−PEO−11.5−0.5 hydrogel. The original mask on the quartz curing attachment (left) has been transferred to the hydrogel after UV curing. Swelling in water dissolved the uncured, masked region, resulting in excellent translation of the star pattern. Notably, the size of the star increases with swelling. The hydrogel was dyed for photographic clarity.

■ EXPERIMENTAL SECTION

Materials and Methods. 1,3-Butadiene (99+%, 100 ppm *p-tert*-butylcatechol inhibitor, Aldrich) was purified by static vacuum (15−30 mTorr) distillations from *n*-butyllithium (1.6 M in hexanes, Aldrich) at −20 °C. Ethylene oxide (99.5+%, compressed gas, Aldrich) was purified by successive distillations from di-*n*-butylmagnesium (1.0 M in heptane, Aldrich) at 3 °C. *sec*-Butyllithium (1.3 M in cyclohexane/hexane, Fisher) was used as received. The concentration before use was determined to be 1.1 M using the double Gilman titration method[50] with 1,2-dibromoethane (99%, Aldrich). Potassium naphthalenide solution was prepared according to a previous report.[30] 3-Chloroperoxybenzoic acid (MCPBA, 70−75%, Acros Organics) was dissolved in methylene chloride and dried over anhydrous sodium sulfate. (4-Iodophenyl)diphenylsulfonium triflate (IPDPST) photoinitiator (Aldrich) and α,α′-dibromo-*p*-xylene (97%, Aldrich) were used as received. Tetrahydrofuran (THF) was degassed by sparging with argon (10 psi) for a period of 45 min and then purified over two molecular sieve columns of neutral alumina (Glass Contour, Inc.). Cyclohexane (CHX) was degassed with argon and purified through a column of neutral alumina followed by a column of Q5 copper(II) oxide catalyst (Glass Contour, Inc.). Other common chemicals and solvents were used as received unless otherwise stated. Ultrahigh purity argon (99.998% Airgas) was passed through a column of 5 Å molecular sieves with drierite (Agilent) and an oxygen-absorbing purifier column (Matheson Trigas). Glassware and polymerization reactors were flamed under vacuum and backfilled with argon (3×).

Measurements. NMR spectra were recorded at room temperature on a Varian Inova 400 MHz spectrometer with a d1 pulse delay of 20 s to ensure complete relaxation of end groups. Spectra were referenced to the residual protio solvent, CHCl$_3$. Gel permeation chromatography (GPC) spectra were collected on a Viscotek GPC-Max chromatography system outfitted with three 7.5 × 340 mm Polypore (Polymer Laboratories) columns in series, a Viscotek differential refractive index (RI) detector, and an Alltech column oven (mobile phase THF, 40 °C, 1 mL min^{-1}). Rheological melt experiments were run on a TA Instruments Advanced Rheometric Expansion System (ARES) rheometer. Copolymer samples were pressed as solid discs (8 × 1 mm, samples for curing were 8.18 × 0.33 mm) at 100 °C with an applied pressure of 500 psi for 60 s. Discs were positioned between two parallel plates (8 mm diameter). The rheometer parallel plates were heated to 75 °C, and the gap was reduced and adjusted to ensure even distribution of the sample. Typical gaps were 0.4−0.6 mm for uncured samples and ~0.3 mm for cured disks. Dynamic temperature ramp tests were performed while heating and cooling at 1 °C min^{-1} at angular frequency of 1 rad s^{-1} and a strain of 1% (well within the linear viscoelastic regime, determined by dynamic strain sweep experiments for each copolymer). Rheological swollen hydrogel frequency sweep experiments were run at room temperature using a Peltier lower tool apparatus and a 25 mm stainless steel upper parallel plate. A slight force was applied (5−10 g) to the hydrogel samples to prevent slip. Strain rates were adjusted depending on the linear viscoelastic regime (0.5−1%). Small-angle X-ray scattering (SAXS) data were collected on a Rigaku S-Max 3000 High Brilliance three pinhole SAXS system outfitted with a MicroMax-007HFM rotating anode (Cu Kα), Confocal Max-Flux Optics, Gabriel multiwire area detector, and a Linkam thermal stage. Dry polymer samples were sandwiched between Kapton windows (0.05 mm thick × 10 mm diameter). Exposure times for uncured samples were typically on the order of 600−1200 s. Cured sample exposure times varied between 1800 and 3600 s. Equilibrium swollen hydrogels were sealed in a Kapton window cell. A shim washer was placed around the swollen hydrogel, and industrial Loctite two-component epoxy glue was used to bond the Kapton film together. After the epoxy glue was fully hardened, DOW Corning high-vacuum grease was applied around the glue seal. Before collecting SAXS data, the Kapton window containing the hydrogel was checked for leaks under high vacuum. The exposure time for swollen hydrogel SAXS was 6−12 h.

ω-Hydroxypolybutadiene (PB). Purified 1,3-butadiene monomer (45.3 g, 12 h) was added very slowly (*caution: if butadiene monomer is added too quickly, the pressure will rise uncontrollably*) over a period of 3 h to a 2 L reactor flask containing 1 L of cyclohexane (40 °C) and *sec*-butyllithium (11.98 mL, 1.1 M) under a slight initial positive pressure of argon (1 psi). During the monomer addition, the pressure was allowed to rise to a maximum of 8 psi. Once the monomer polymerized and the pressure dropped below 3 psi, more butadiene monomer was added. Ethylene oxide (12.6 g, 20 h) was used as an end-capping agent. After purging the reactor of excess ethylene oxide, the terminal alkoxide was quenched with wet methanol (26 mL, 25:1 MeOH−H$_2$O). The homopolymer was washed (2×) with 250 mL of deionized H$_2$O and precipitated from 3:1 MeOH−EtOH (8 L). The product was dissolved in benzene and freeze-dried in vacuo (25 °C, 72 h). Recovered sticky clear viscous liquid, 42.0 g (93%). GPC (polystyrene standards): $M_w/M_n = 1.05$. ^{1}H NMR (400 MHz, CDCl$_3$, δ): 5.3−5.7 (b, $-\mathrm{CH_2}-\mathrm{C}H{=}\mathrm{C}H-\mathrm{CH_2}-$ and $\mathrm{CH_2}{=}\mathrm{C}H-\mathrm{CH}-$), 4.9−5.1 (b, $\mathrm{C}H_2{=}\mathrm{CH}-$), 3.6−3.7 (m, $-\mathrm{C}H_2-\mathrm{OH}$), 1.7−2.3 (b, $-\mathrm{C}H_2-\mathrm{CH}{=}\mathrm{CH}-\mathrm{C}H_2-$ and $\mathrm{CH_2}{=}\mathrm{CH}-\mathrm{C}H-$), 1.1−1.7 (b, $\mathrm{CH_2}{=}\mathrm{CH}-\mathrm{C(R)H}-\mathrm{C}H_2-$), 0.8−0.9 (m, $\mathrm{C}H_3-\mathrm{CH_2}-\mathrm{C(R)H}-\mathrm{C}H_3$, initiator fragment). M_n (calcd from ^{1}H NMR integrations) = 3300 g mol^{-1}; 1,2 content = 8.3%.

ω-Hydroxypolybutadiene-*b*-poly(ethylene oxide) (PB−PEO). PB (3.2 g) was dissolved in 250 mL of THF and added via cannula to a 2 L reactor flask containing 800 mL of THF at 40 °C. PB alkoxide chain ends were formed by titrating the solution with potassium naphthalenide slowly until a light green color remained for at least 5 min. Ethylene oxide (26.4 g, 24 h) was added to the reactor under a slight positive pressure of argon (1 psi); the solution turned clear after several seconds. The reactor was quenched with wet methanol (20 mL, 3:1 MeOH−H$_2$O), and the solution changed color from charcoal blue to rose red immediately. The polymeric solution was reduced to ~1/2 its volume on a rotoevaporator. The block copolymer alcohol product precipitated from −20 °C pentane (4 L). Filtration and drying in vacuo (25 °C, 24 h) gave the block copolymer as a light tan powder. Yield = 26.6 g (90%). GPC (polystyrene standards): $M_w/M_n = 1.03$. ^{1}H NMR (400 MHz, CDCl$_3$, δ): 5.2−5.6 (b, $-\mathrm{CH_2}-\mathrm{C}H{=}\mathrm{C}H-\mathrm{CH_2}-$ and $\mathrm{CH_2}{=}\mathrm{C}H-\mathrm{CH}-$), 4.8−5.0 (b, $\mathrm{C}H_2{=}\mathrm{CH}-$), 3.3−3.9 (b, $-\mathrm{C}H_2-\mathrm{C}H_2-\mathrm{O}-$), 1.6−2.3 (b, $-\mathrm{C}H_2-\mathrm{CH}{=}\mathrm{CH}-\mathrm{C}H_2-$ and $\mathrm{CH_2}{=}\mathrm{CH}-\mathrm{C(R)}H-$, 1.0−1.5 (b, $\mathrm{CH_2}{=}\mathrm{CH}-\mathrm{C(R)H}-\mathrm{C}H_2-$), 0.7−0.9 (m, $\mathrm{C}H_3-\mathrm{CH_2}-\mathrm{C(R)H}-\mathrm{C}H_3$, initiator fragment). $f_{\mathrm{PB}} = 0.13$, M_n = 29 500 g mol^{-1} (calcd from ^{1}H NMR integrations).

Polybutadiene-*b*-poly(ethylene oxide)-*b*-polybutadiene (PB−PEO−PB). PB−PEO (4.3 g) was dissolved in 50 mL of THF and titrated to a light green color with potassium naphthalenide under argon. α,α′-Dibromo-*p*-xylene was dissolved in THF (0.50 mL, 0.6 M, 1:0.5 equiv of PB−PEO: α,α′-dibromo-*p*-xylene) and was added at a rate of 0.1 mL h^{-1} with a Chemyx Fusion 200 syringe pump to the titrated PB−PEO flask. The copolymer mixture precipitated from −20 °C pentane (1.5 L). Filtration and drying in vacuo (25 °C, 48 h) gave the copolymer as a light yellow rubbery powder. Yield = 3.7 g (86%). The copolymer mixture was 89.6% triblock by mass (calcd from GPC peak integrations).

Epoxidation of PB−PEO/PB−PEO−PB Blends (ePB$_{19.6}$−PEO−11.5). PB−PEO−PB triblock mixture (0.5 g) and PB−PEO (1.96 g) were codissolved in 40 mL of CH$_2$Cl$_2$. The copolymer mixture represents an 11.5 mol % triblock composition. Controlled partial epoxidation was carried out with MCPBA (0.231 g) described in a previous report by Scalfani and Bailey.[30] An additional purification step of precipitating from pentane (1 L) was added to the procedure. Filtration and drying in vacuo (25 °C, 48 h) gave the epoxidized copolymer as an off-white powder. Yield = 2.15 g (87%). GPC (polystyrene standards): $M_w/M_n = 1.15$ (bimodal due to intentional blending with triblock). ^{1}H NMR (400 MHz, CDCl$_3$, δ): 7.3 (s, $-\mathrm{O}-\mathrm{CH_2}-\mathrm{C_6}H_4-\mathrm{CH_2}-\mathrm{O}-$, coupling agent) 5.2−5.6 (b, $-\mathrm{CH_2}-\mathrm{C}H{=}\mathrm{C}H-\mathrm{CH_2}-$ and $\mathrm{CH_2}{=}\mathrm{C}H-\mathrm{CH}-$), 4.8−5.0 (b, $\mathrm{C}H_2{=}\mathrm{CH}-$), 4.5 (s, $-\mathrm{O}-\mathrm{C}H_2-\mathrm{C_6H_4}-\mathrm{C}H_2-\mathrm{O}-$), 3.3−4.0 (b, $-\mathrm{C}H_2-\mathrm{C}H_2-\mathrm{O}-$), 2.8−3.0 (b, $-\mathrm{CH_2}-\mathrm{C}H\mathrm{(O)C}H-\mathrm{CH_2}-$, epoxidized 1,4 cis), 2.6−2.7 (b, $-\mathrm{CH_2}-\mathrm{C}H\mathrm{(O)C}H-\mathrm{CH_2}-$, epoxidized 1,4 trans), 1.0−2.3 (b, $-\mathrm{C}H_2-\mathrm{CH}{=}\mathrm{CH}-\mathrm{C}H_2-$, $-\mathrm{C}H_2-\mathrm{CH(O)CH}-\mathrm{C}H_2-$, $\mathrm{CH_2}{=}\mathrm{CH}-\mathrm{C(R)}H-$, $\mathrm{CH_2}{=}\mathrm{CH}-\mathrm{C(R)H}-\mathrm{C}H_2-$), 0.7−0.9 (m, $\mathrm{C}H_3-\mathrm{CH_2}-\mathrm{C(R)H}-\mathrm{C}H_3$, initiator fragment). Epoxidized units: total = 19.6%, 1,4 cis = 9.8%, 1,4 trans = 9.8%, 1,2 = 0% (calcd from ^{1}H NMR integrations).

Photocuring of ePB$_{19.6}$−PEO−11.5−0.5. ePB$_{19.6}$−PEO−11.5 samples were codissolved with 0.5 mol % (relative to initial PB repeat units) (4-iodophenyl)diphenylsulfonium triflate in a 3:1 benzene−chloroform mixture and freeze-dried overnight. Samples were pressed as 8.18 mm × 0.33 mm discs at 100 °C for 60 s and then quenched in liquid nitrogen to minimize crystallization-induced roughening of the surface. Discs were placed on a TA Instruments ARES rheometer outfitted with a Peltier and a reflecting mirror on a quartz parallel plate (Kapton film was used in-between the sample and Peltier attachment to prevent sticking). The quartz attachment was aligned to be 0.5 mm from the surface of the sample. A Hamamatsu Lightning Cure LC8 UV spot cure system was utilized with a 200 W mercury−xenon lamp, synthetic silica light guide, and short focal point condenser lens. The light guide was positioned ~1 cm from the upper quartz reflecting mirror. The lamp was allowed to stabilize for 15 min before curing. The intensity at the cure site was 95−103 mW cm^{-2} (measured in the range of 230−410 nm with a Con-Trol-Cure Silver Line UV-radiometer). Prior to cure, the samples were heated to 140 °C on the Peltier and then cooled to the curing temperature of 100 °C. Samples were exposed to UV light for 4−5 min. After curing, the discs became mechanically rigid, insoluble, and light amber in color.

ASSOCIATED CONTENT

Ⓢ **Supporting Information.** Temperature-dependent SAXS of PB−PEO−11.5 and ePB$_{19.6}$−PEO−11.5 (Figures S1 and S2); evolution of S$_{BCC}$ morphology after low temperature 80 °C annealing (Figure S3); FT-IR comparison of PB−PEO−11.5 and ePB$_{19.6}$−PEO−11.5 (Figure S4). This material is available free of charge via the Internet at http://pubs.acs.org.

AUTHOR INFORMATION

Corresponding Author

*E-mail: travis.bailey@colostate.edu.

ACKNOWLEDGMENT

This work was supported by the National Science Foundation (Grant DMR-0645781) and the Colorado State University. The SAXS instrument at CSU is supported by the Central Instrument Facility of the Chemistry Department and the National Science Foundation MRI Program (Grant DMR-0821799). V.F.S. would like to thank M.L.S. for helpful discussions.

REFERENCES

(1) Hoare, T. R.; Kohane, D. S. *Polymer* **2008**, *49* (8), 1993–2007.

(2) Slaughter, B. V.; Khurshid, S. S.; Fisher, O. Z.; Khademhosseini, A.; Peppas, N. A. *Adv. Mater.* **2009**, *21*, 3307–3329.

(3) Tokarev, I.; Minko, S. *Adv. Mater.* **2010**, *22*, 3446–3462.

(4) Wang, C.; Varshney, R. R.; Wang, D.-A. *Adv. Drug Delivery Rev.* **2010**, *62* (7−8), 699–710.

(5) Zohuriaan-Mehr, M.; Omidian, H.; Doroudiani, S.; Kabiri, K. *J. Mater. Sci.* **2010**, *45* (21), 5711–5735.

(6) Peppas, N. A.; Hilt, J. Z.; Khademhosseini, A.; Langer, R. *Adv. Mater.* **2006**, *18* (11), 1345–1360.

(7) Desai, P. N.; Yuan, Q.; Yang, H. *Biomacromolecules* **2010**, *11* (3), 666–673.

(8) Galperin, A.; Long, T. J.; Ratner, B. D. *Biomacromolecules* **2010**, *11* (10), 2583–2592.

(9) Hou, Y.; Schoener, C. A.; Regan, K. R.; Munoz-Pinto, D.; Hahn, M. S.; Grunlan, M. A. *Biomacromolecules* **2010**, *11* (3), 648–656.

(10) Lee, K. Y.; Mooney, D. J. *Chem. Rev.* **2001**, *101* (7), 1869–1880.

(11) Stile, R. A.; Burghardt, W. R.; Healy, K. E. *Macromolecules* **1999**, *32* (22), 7370–7379.

(12) Xu, Y.; Sato, K.; Mawatari, K.; Konno, T.; Jang, K.; Ishihara, K.; Kitamori, T. *Adv. Mater.* **2010**, *22* (- 28), 3017–3021.

(13) Kozlovskaya, V.; Sukhishvili, S. A. *Macromolecules* **2006**, *39* (18), 6191–6199.

(14) Dai, H.; Chen, Q.; Qin, H.; Guan, Y.; Shen, D.; Hua, Y.; Tang, Y.; Xu, J. *Macromolecules* **2006**, *39* (19), 6584–6589.

(15) Gong, C.; Shi, S.; Wang, X.; Wang, Y.; Fu, S.; Dong, P.; Chen, L.; Zhao, X.; Wei, Y.; Qian, Z. *J. Phys. Chem. B* **2009**, *113* (30), 10183–10188.

(16) Annaka, M.; Matsuura, T.; Kasai, M.; Nakahira, T.; Hara, Y.; Okano, T. *Biomacromolecules* **2003**, *4* (2), 395–403.

(17) Susanto, H.; Ulbricht, M. *Langmuir* **2007**, *23* (14), 7818–7830.

(18) Tokuyama, H.; Iwama, T. *Langmuir* **2007**, *23* (26), 13104–13108.

(19) Calvert, P. *Adv. Mater.* **2009**, *21* (7), 743–756.

(20) Bates, F. S. *Science* **1991**, *251* (4996), 898–905.

(21) Bates, F. S.; Fredrickson, G. H. *Phys. Today* **1999**, *52*, 32–38.

(22) He, C. L.; Kim, S. W.; Lee, D. S. *J. Controlled Release* **2008**, *127* (3), 189–207.

(23) Minh, K. N.; Lee, D. S. *Macromol. Biosci.* **2010**, *10* (6), 563–579.

(24) Vermonden, T.; Besseling, N. A. M.; van Steenbergen, M. J.; Hennink, W. E. *Langmuir* **2006**, *22* (24), 10180–10184.

(25) Sanabria-DeLong, N.; Crosby, A. J.; Tew, G. N. *Biomacromolecules* **2008**, *9* (10), 2784–2791.

(26) Censi, R.; Vermonden, T.; Deschout, H.; Braeckmans, K.; di Martino, P.; De Smedt, S. C.; van Nostrum, C. F.; Hennink, W. E. *Biomacromolecules* **2010**, *11* (8), 2143–2151.

(27) Guo, C.; Bailey, T. S. *Soft Matter* **2010**, *6* (19), 4807–4818.

(28) Nykaenen, A.; Nuopponen, M.; Laukkanen, A.; Hirvonen, S.P.; Rytelae, M.; Turunen, O.; Tenhu, H.; Mezzenga, R.; Ikkala, O.; Ruokolainen, J. *Macromolecules* **2007**, *40* (16), 5827–5834.

(29) Xu, C.; Fu, X.; Fryd, M.; Xu, S.; Wayland, B. B.; Winey, K. I.; Composto, R. J. *Nano Lett.* **2006**, *6* (2), 282–287.

(30) Scalfani, V. F.; Bailey, T. S. *Chem. Mater.* **2010**, *22* (21), 5992–6000.

(31) Crivello, J. V. *Annu. Rev. Mater. Sci.* **1983**, *13*, 173–190.

(32) Crivello, J. V. *J. Polym. Sci., Part A: Polym. Chem.* **1999**, *37*, 4241–4254.

(33) For a detailed overview comparing classic BCP cross-linking strategies to cationic photoinitiators, see ref 30.

(34) Hillmyer, M. A.; Bates, F. S. *Macromolecules* **1996**, *29* (22), 6994–7002.

(35) Hsieh, H. L.; Quirk, R. P. *Anionic Polymerization, Principles and Practical Applications*; Marcel Dekkar, Inc.: New York, 1996.

(36) Kossuth, M. B.; Morse, D. C.; Bates, F. S. *J. Rheol.* **1999**, *43* (1), 167–196.

(37) Mai, S.-M.; Mingvanish, W.; Turner, S. C.; Chaibundit, C.; Fairclough, J. P. A.; Heatley, F.; Matsen, M. W.; Ryan, A. J.; Booth, C. *Macromolecules* **2000**, *33* (14), 5124–5130.

(38) Matsen, M. W.; Thompson, R. B. *J. Chem. Phys.* **1999**, *111* (15), 7139–7146.

(39) Fetters, L. J.; Lohse, D. J.; Richter, D.; Witten, T. A.; Zirkel, A. *Macromolecules* **1994**, *27* (17), 4639–4647.

(40) Floudas, G.; Vazaiou, B.; Schipper, F.; Ulrich, R.; Wiesner, U.; Iatrou, H.; Hadjichristidis, N. *Macromolecules* **2001**, *34* (9), 2947–2957.

(41) Müller, A.; Balsamo, V.; Arnal, M. Nucleation and Crystallization in Diblock and Triblock Copolymers. In *Block Copolymers II*; Abetz, V., Ed.; Springer: Berlin, 2005; Vol. 190, pp 1−63.

(42) Cavicchi, K. A.; Lodge, T. P. *Macromolecules* **2003**, *36* (19), 7158–7164.

(43) Kinning, D. J.; Thomas, E. L. *Macromolecules* **1984**, *17* (9), 1712–1718.

(44) Schwab, M.; Stuhn, B. *Phys. Rev. Lett.* **1996**, *76* (6), 924.

(45) Wang, X.; Dormidontova, E. E.; Lodge, T. P. *Macromolecules* **2002**, *35* (26), 9687–9697.

(46) Yamaguchi, D.; Hashimoto, T.; Vaidya, N. Y.; Han, C. D. *Macromolecules* **1999**, *32* (22), 7696–7699.

(47) Lee, S.-H.; Char, K.; Kim, G. *Macromolecules* **2000**, *33* (19), 7072–7083.

(48) De Risi, F. R.; D'Ilario, L.; Martinelli, A. *J. Polym. Sci., Part A: Polym. Chem.* **2004**, *42* (12), 3082–3090.

(49) Dissanayake, M. A. K. L.; Frech, R. *Macromolecules* **1995**, *28* (15), 5312–5319.

(50) Gilman, H.; Cartledge, F. K. *J. Organomet. Chem.* **1964**, *2* (6), 447–454.